Heliyon 10 (2024) e35643

Contents lists available at ScienceDirect

Heliyon

journal homepage: www.cell.com/heliyon

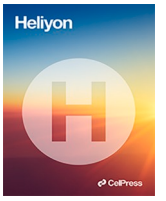

Research article

In-situ grown ternary metal hydroxides@3D oriented crumpled V_2C MXene sheets for improved electrocatalytic oxygen evolution reaction

Anum Iqbal [a], Hamzeh Sabouni [a], Nasser M. Hamdan [a,b,*]

[a] *Material Science and Engineering Program, The American University of Sharjah, Sharjah, 26666, United Arab Emirates*
[b] *Physics Department, The American University of Sharjah, Sharjah, 26666, United Arab Emirates*

ARTICLE INFO

Keywords:
Three-dimensional (3D) crumpled sheets
V_2C MXene
Trimetallic hydroxides
OER kinetics
And freeze drying

ABSTRACT

High valence multi transition metal hydroxides are greatly enriched with OER redox active sites due to strong synergy of heteroatomic nuclei. The efficiency of these redox active sites could be efficiently improved by coupling with highly conductive substrate. The advanced three-dimensional (3D) architecture and hydrophilic terminal functionalities of MXene (MX) considerably enhance the maximum utilization rate of anchored redox active sites by triggering the direct growth of these at MX substrate. Here-in, the freeze-dried 3D network of crumpled Vanadium-Carbide (V_2C) MX sheets regulates the crystallization of in-situ grown NiFeCr multi transition metal hydroxides on MX scaffold through co-precipitation process. The XPS results suggest a synergistic chemical interaction of 3D MX scaffold with NiFeCr that modifies the electronic structure of the composite ensuring reduced charge transfer resistance. Besides, as found in FESEM morphological investigation, the well-dispersed NiFeCr multi-transition metal hydroxides are immobilized on open pores like structure of V_2C-MX facilitate thoroughly accessible active sites. As a result, the NiFeCr@3D V_2C-MX composite has shown an excellent electrocatalytic activity with an overpotential of 410 mV at a current density of 200 mA cm^{-2}, Tafel slope of 100 mV dec in 1M KOH. Besides, the significant interaction between metallic centers and MXene support prevent detachment or agglomeration of active centers providing maximum interaction with the electrolytic ions, quick ionic OH^- transportation, speedy and stable electron transfer channels thus ensure the long-term stability of NV-5MX during 53 h continuous operation of OER. Furthermore, we have utilized a more accurate value of half-cell standard reduction potential of the Hg/HgO electrode in the Nernst equation to represent all test voltages and to determine the overpotential values. In essence, this study features a facile approach for the confined growth of multi transition metal hydroxides in the presence of morphologically unique 3D crumpled V_2C MXene architectures. Consequently, the increased OER reaction kinetics and improved stability of the synthesized composites are potentially due to synergistic interplay between well dispersed active sites and the conductive substrate.

* Corresponding author. Material Science and Engineering Program, The American University of Sharjah, Sharjah, 26666, United Arab Emirates.
E-mail address: nhamdan@aus.edu (N.M. Hamdan).

https://doi.org/10.1016/j.heliyon.2024.e35643
Received 13 May 2024; Received in revised form 31 July 2024; Accepted 1 August 2024
Available online 3 August 2024

1. Introduction

In renewable green energy production, various complex chemical reactions occur at an electrochemical interface composed of an electrode and an electrolyte, such as adsorption/desorption phenomena, electron-and charge-transfer and solvation and desolvation processes. The functionality of these electrode/electrolyte interfaces is a key factor for the required performance of modern energy harvesting devices including electrochemical water splitting and metal-air batteries. The reactions at this interface are highly dependent upon surface electronic and geometric characteristics of the electrode material [1]. The oxygen evolution reaction (OER), a half-cell reaction in metal-air batteries and water splitting, involves four electron transfer and the formation of multiple intermediates at the electrode surface thus causing a comparatively higher overpotential [2–4]. The focus of most research in electrocatalysis is haunting new electrocatalysts with superior electrocatalytic performance, in terms of high activity and stability.

Transition metal elements are advantageous due to low cost, abundant availability, and good theoretical catalytic activity. Fundamentally, the OER mechanism on transition metal-based composites initiates with the adsorption of hydroxyl radical on active transition metal sites (M) to form M − OH bond. This M − OH bond is transformed into M − O through coupled proton and electron removals. The further nucleophilic interaction of OH^- on M − O with e^- oxidation generates the hydroperoxide intermediate M-OOH. Finally, a proton-coupled electron conduction facilitates the oxygen evolution and the regeneration of free active site. Thereby, M − OH bond strength determines the efficiency of oxygen evolution reaction kinetics. Theoretically, the d-electrons of transition metal interacts with the antibonding orbitals of the M − OH bond. The highly enriched d-electrons weakens the bonding of M − OH, thus enhancing the OER performance [5]. However, an optimized M − OH bond-strength is required for appreciable OER kinetics involving absorption of OH^- ions and the formation of oxygen intermediates. The M − OH binding strength of mono-transition metal hydroxides can be optimized by mixing with other hetero-nuclei transition metals.

Layered double hydroxide (LDH) is a two-dimensional (2D) layered material with general formula of $\{M^{+2}_{1-x}M^{+3}_{x}(OH)_2\}\ (A^{n-})_{x/n}.mH_2O$ where M^{+2} are divalent and M^{+3} trivalent metal ions in the main layer, and A^{n-} is the interlayer anion for charge compensation. The adjustable composition and tunable electronic structures of the metal $–O_6$ ($M–O_6$) octahedral local framework are the active centers for oxygen evolving process [6]. The insertion of multiple transition metals in this structure provides metal oxidation states in the given potential window, thus improving the electro-catalytic performance [7,8]. Although the hetero nuclei provide chemically diverse redox active sites, the complete utilization of these active sites is another crucial factor for improved OER kinetics [9–12]. Fortunately, the insertion of electrically conductive support with high surface area is a promising approach to induce unique morphological features in hybrid providing high accessibility to the active sites and rapid charge transfer, leading to the enhancement of the catalytic activity [13].

MXenes (MX), an intriguing member of two-dimensional (2D) nanomaterials, is presented by an empirical formula $M_{n+1}X_nT_x$(n = 1–4), where M represents the transition metal, X could be a carbon, nitride or a carbonitride, whereas T refers to the surface terminal groups [14–16]. MX holds exotic features as a support material to immobilize the electrocatalytically active sites for improved OER kinetics. These features are listed as follows [17]; (i) Enlarged surface area with restricted electron movement within ultra-thin 2D sheets, causing MX to possess good metallic conductivity, (ii) the high electronegativity and relatively low work function of MX cause synergistic electron transfer within the composite, thus modifies the electronic scaffold of the hybrid and provides an intense interface interaction for reduced thermodynamic barrier and fast reaction kinetics [18]; (iii) contrast to hydrophobic carbonaceous materials such as graphene, MXenes are more favorable for aqueous electrocatalytic application due to their hydrophilic surface functional groups, reinforcing the maximum adsorption of electrolytic ions at MXene based interfaces [19](iv) The terminal functionalities of MX are used to anchor electrocatalytically active sites and regulate their directed growth at conductive MX substrate with suppressed agglomeration thus providing better corrosion resistance than other carbon-based carriers [20]. However, the defect density and enlarged surface area inevitably co-exist with numerous dangling bonds that lead to strong interlayer stacking and aggregation. Therefore, in order to ensure long-term stability of MX-based electrode, the re-stacking issue of MX sheets is required to be addressed properly. Besides, the oxidation of MX in an aquatic environment or at high voltages degrades its electrical conductance. The self-stacking behavior of MX sheets can be minimized effectively through intercalation of other substances, constructing porous structures, and forming three-dimensional (3D) scaffold [21]. Moreover, due to their appealing tendency for interfacial coupling and charge transfer, MXenes are broadly employed to load catalysts in composite formation, which not only suppresses the MX re-stacking issue, but also leads the uniform growth of catalytic centers and enhances their utilization rate [18].

By keeping all these facts under consideration, herein, we report the synthesis of 3D network of highly crumpled Vanadium Carbide V_2C MX sheets to use as a catalytic support material for improved oxygen evolution kinetics. The 3D crumpled MX sheets are synthesized through etching of V_2AlC MAX phase by using mixed acid HF: HCl etchant solution. The etched sheets are successfully delaminated by using TEA as an intercalating etchant and subsequently MX sponge is obtained by vacuum assisted freeze drying of the MX suspension. Furthermore, the catalytically active NiFeCr trimetal hydroxides are in-situ grown over 3D crumpled MX substrate to attain well dispersed OER catalytically active centers.

Moreover, the OER activity of unary, binary, and ternary metal hydroxides have been evaluated in an alkaline media. In accordance with the previous literature, the NiFe binary metal hydroxides has exhibited increased OER activity as compared to unary and other bimetallic hydroxide. It has been found that the Fe sites with a tuned electronic structure in NiFe can effectively stabilize the OER intermediates by forming O-bridge Fe–Ni reaction centers due to electrostatic synergy of nearby Ni sites [22,23]. Besides, the incorporation of other heteroatoms into the NiFe-LDH greatly influence the neighbouring NiFe sites, particularly in case of high-valence dopants [24,25]. Therefore, considerably increased OER activity of coprecipitated NiFeCr trimetal hydroxides has been achieved. The XRD findings support that Cr^{+3} addition has drastically reduced the crystallinity and enhanced the catalytic

performance due to the amorphous nature of trimetal hydroxides [26]. The lower overpotential of NiFeCr could be attributed to the unique electron configuration ($t_{2g}^{3}e_{g}^{o}$) of Cr which is advantageous for an improved electrocatalytic performance because it facilitates charge transfer and electron capture [27]. Finally, the OER active centers of NiFeCr-LDHs are in situ grown on V_2C MX sheets (NV-$_y$MX) under alkaline environment and heat flux. Notably, the chemical constituents of the NiFeCr@3D crumpled V_2C MX (NV-$_y$MX) catalysts are adjusted, by loading four different contents of V_2C MX sheets, designated as NV-5MX (5 mg V_2C MX), NV-10MX (10 mg V_2C MX), NV-15MX (15 mg V_2C MX), and NV-30MX (30 mg V_2C MX). Consequently, an optimized NV-MX exhibited eximious OER activity in terms of low overpotentials at higher current densities, small Tafel slopes, and long-term stability, prominently superior in comparison of pristine NiFeCr and RuO_2 catalysts.

2. Experimental section

2.1. Materials

Vanadium Aluminium Carbide V_2AlC MAX phase, and Nickel (Ni) Foam were provided from Nanografi. The other chemicals including Hydrofluoric acid (HF), Hydrochloric acid (HCl), Ammonia Solution (25 %), Ethylene Glycol, Nickel (II) Nitrate hexahydrate $NiCl_2.6H_2O$, Iron (III) Nitrate nano-hydrate $Fe(NO_3)_3{\cdot}9H_2O$, Chromium (III) Nitrate nano-hydrate $Cr(NO_3)_3{\cdot}9H_2O$, Carbon black, Nafion 5 wt%, Ethanol, Nitric acid, and triethylamine (TEA) were purchased from Sigma-Aldrich. No further purification was needed for the consumption of materials.

2.2. Synthetic protocols

2.2.1. Synthesis of V_2C MXene

Typically, V_2AlC was etched in 48 wt% hydrofluoric acid (HF). HF is a harsh etching media and usually yields defect enriched MX multilayers and flakes. Therefore, to preserve the material's integrity, a mild etching solution of mixed HF and HCl was used to synthesize V_2CT_x. Typically, the etching was carried out in a loosely closed high-density polyethylene (HDPE) vessel. 1 g of V_2AlC was put into mixed 12 mL of 48 wt% HF and 8 mL of 12 M HCl solution under ice cooled water bath for a few minutes at uniform stirring rate of 200 rpm. After a while, the mixture was then subjected to etching at constant 50 °C temperature provided through heated oil container for 72 h under continuous stirring of 400 rpm. Upon the completion of etching, the mixture was then poured in 50 mL centrifuge vials for centrifugation initially at 3000 rpm for 5 min. At this stage, the ml-V_2C along with some amount of MAX phase was settled at the bottommost part of the vials, whereas greenish liquid containing vanadium ions was obtained. The etched MX ml-V_2C phase was neutralized with N_2 purged DI water and centrifuged several times to attain the pH $>$ 5. For 1g of etched yield, the washing procedure typically consumes $>$1.5 L of DI water. The wet paste of etched MX ml-V_2C phase was immediately delaminated into 10 % TEA suspension (1 g/20 mL) at ambient conditions and stirred for 6h. Later the solution is then diluted with 200 ml DI H_2O and freeze dried. Prior to freeze drying, the diluted solution of delaminated MX phase was freezed in liquid N_2 for 5 min and then subjected to a vacuum drying machine under $1x10^{-3}$atm at −85 °C for 96 h. The obtained freeze-dried sponge exhibits a brownish tinge in comparison to gray MAX phase. The detailed schematics of MX synthesis has been illustrated in Supplementary Fig. S1A.

2.2.2. Synthesis of NiFeCr-LDHS and NiFeCr@V_2C MX

The NV-$_y$MX catalysts with different amount of MX sheet loadings were fabricated through in-situ coprecipitation of NiFeCr on 3D crumpled MX sheets in an open oil bath as presented in schematics 1. The typical synthesis of NV-5MX involved the preparation of suspension 1 by sonicating the 5 mg V_2C-MX sheets in 10 ml N_2 purged deionized water until all the MXene sheets were well dispersed. The different proportions of $NiCl_2.6H_2O$, $Fe(NO_3)_3{\cdot}9H_2O$, and $Cr(NO_3)_3{\cdot}9H_2O$ in accordance with the molar ratio $Ni_{0.75}$:$Fe_{0.15}$:$Cr_{0.10}$ were added to 70 ml mixed solution of DI-H_2O:Ethylene glycol with the volume ratio of (6:1) referred as suspension 2. Next, the suspension 1 was added dropwise into the suspension 2 and kept under stirring for 30 min at room temperature. After the proper mixing of both suspensions, the mixed solution was stirred at 80 °C for 15 min in an oil bath. The desired temperature was attained progressively by raising 10 °C in 5 min intervals. Subsequently, the in-situ coprecipitation of NiFeCr ions on inserted V_2C-MX sheets were initiated by adding 1.5 ml of ammonia solution. During the dropping process, the pH of the mixture was adjusted to 8. The mixed suspension was vigorously stirred under the same reaction conditions for 2 h. The suspension was then cooled at ambient conditions, the particles were collected by various centrifugation-rinsing cycles initially with deionized water and final washing was with ethanol to remove any organic impurities. The resultant paste was then solidified through over-night heating at 80 °C in vacuum drying oven. The granules were then crushed into fine powder by using agate motor-pestle. According to the different contents of V_2C-MX sheets, the samples were marked as NV-$_5$MX, NV-$_{10}$MX, NV-$_{15}$MX, and NV-$_{30}$MX. Similarly, other catalysts including $Ni(OH)_2$, NiCr-LDHs, NiFe-LDHs, and NiFeCr-LHs were also prepared through above mentioned synthetic protocol but without adding MXene contents.

2.3. Material characterization

X-ray diffracted (XRD) reflections were crecorded through a BRUKER D8-ADVANCE powder diffractometer that includes a monochromatized Cu Kα radiation (λ = 1.5406 Å). The powder samples were prepared on a flat sample holder. The device input electrical parameters were set as 30 mA current and 40 kV accelerated voltage. The diffracted rays were captured by the increments of 0.03 over a wide range of 2ɵ values from 3° to 80°. The "Joint Committee on Powder Diffraction Standards" (JCPDS) data were used to examine

the crystallographic phase identification. The crystallite sizes (Supplementary Fig. S1C) are estimated through Scherrer equation Eq. (1) where D is the average crystallite size, K = 0.9 for spherical particles, β is the peak broadening of full width at half-maximum intensity (FWHM) of the most intense peak. The Raman measurements have been conducted on a HORIBA microscope fitted with He–Ne 17 mW, λ = 633× nm red laser source and 50 × objective lens. The micromorphology and elemental composition of the synthesized catalysts were characterized by Field Emission Electron Microscope (FESEM-Nova Nano SEM 450, USA) equipped with Energy dispersive X-Ray spectroscopy (EDX-INCA 250 X-Max 50, England) at an accelerating voltage of 1 and 15V respectively. For FESEM and EDX, the suspension of the catalyst powder was drop-casted on a silicon wafer. The chemical states of the electrocatalysts were evaluated through X-Ray Photoelectron Spectrometer (XPS) based upon Al (K-alpha) source with operating parameters of 15 keV and 15 mA. The analysis chamber was maintained at a pressure $< 5 \times 10^{-9}$ mbar. Moreover, the XPS spectra were calibrated to the binding energy of C1s at 284.8 eV.

$$D = \frac{k\lambda}{\beta \cos\theta} \tag{1}$$

2.4. Electrochemical testing

The required electrochemical techniques were executed through a Biologic VSP-200 electrochemical workstation at ambient conditions in 1M KOH using a common three-electrode system consisting of 1cmX1cm Platinum plate, Ni foam, and 1M Hg/HgO electrode acting as the auxiliary, anodic, and reference electrodes separately. The working electrode preparation was completed by sonicating 5 mg catalyst, 5 mg carbon black, and 50 μL 5 wt% Nafion solution into the mixed solution (1:1 vol) of ethanol and deionized water for 1 h. A fixed volume of 30 μL of the catalyst ink was then deposited onto the pre-treated Ni foam of (0.5 cmX0.5 cm) dimensions which was subsequently dried at 60 °C under vacuum. For the acidic treatment, the Ni foam was cleaned sequentially with ethanol and DI water for 10 min sonication time. Then the washed Ni foam was treated with 6MHCl solution for 30 min at room temperature to remove the surface oxide layer. After that, the pH of Ni foam was neutralized with several DI water washings. Prior to the deposition, the Ni foam was dried at 45 °C under vacuum.

High-purity N_2 gas was purged into the KOH electrolyte for 30 min before conducting the OER electrochemical measurements. Before analyzing the OER performance, the working electrodes were activated through several cyclic voltammetry (CV) curves at a scanning speed of 100 mV/s in the same electrolyte used for OER measurement. The LSV curves were obtained at the scanning speed of 10 mV/s with 85 % iR compensation through AUTOLAB software. The chronoamperometry was performed to anticipate the stability of electrode material at constant activated potentials. The Electrochemical impedance spectroscopy (EIS) was performed from 100 MHz to 0.1 Hz, with an AC disturbance voltage of 5 mV. The impedance data were fitted in accordance with the Randles circuit to extract the solution and electron-conduction resistances. The testing voltage window was presented into reversible hydrogen electrode (RHE) voltage in accordance with the Nernst Eq. (2) [28], where pH ~ 13.8, $E^{\ominus real}_{Hg/HgO\ 1M\ KoH} = 110.0$ mV which is higher than the 98.3 mV used in other reported literature. This is recently provided more accurate value of $E^{\ominus real}_{Hg/HgO\ 1M\ KoH}$ incorporating the effect of OH^- ions of the internal solution in the Hg/HgO electrode [29].

$$E_{RHE} = E_{Hg/HgO} + 0.059pH + E^{\ominus real}_{Hg/HgO\ 1M\ KoH} \tag{2}$$

To evaluate the kinetic performance of the synthesized catalysts, the Tafel slope was extracted through linear fitting of the Tafel plots in accordance with the Tafel Eq. (3) where η is the iR-free potential, b is the Tafel slope, j is the current density and a is the constant [30].

$$\eta = a + b\log(j) \tag{3}$$

the product of scan rate ν and electrochemical double-layer capacitance C_{dl} results into the double-layer charging current I_C, as given in Eq. (4) [28]. Thus, the slope of the linear fit for I_c versus ν represents the C_{dl} value. Here-in, the C_{dl} values were estimated through cyclic voltammogram (CV) at varying scan rates (20, 40, 60, 80, 100 mV/s) within the non-faradaic potential range (V vs. RHE) through plotted $j = (j_p - j_n)/2$ at mid-point of the potential window versus the scan rate where j_p and j_n represent the anodic and cathodic current density, respectively. The electrochemical active surface area (ECSA) of the catalyst was determined using Eq. (5), where specific capacitance (C_s) is 0.040 mF cm^{-2} [31,32].

$$I_c = \nu C_{dl} \tag{4}$$

$$ECSA = \text{Geometrical Surface area} \times \frac{C_{dl}}{C_s} \tag{5}$$

3. Results and discussion

Foremost, the MXene nanosheets were fabricated through mixed-acid etching, delamination and freeze-casting processes. There are two essential stages in freeze casting known as freezing and freeze-drying. In an initial freezing phase, the precursor solution consisting of solvent and solute particulates is frosted in a container to attain a specified form. While getting frozen, the solute particulates are

repelled due to the growth of solvent crystals resulting into a dense framework of solute particles. Then the freeze solvent crystals are sublimated upon low temperature and pressure, and a porous framework reflecting the morphology of the solvent crystals can be achieved [33,34]. Therefore, in the present study the suspension was kept in a cylindrical quartz jar with a diameter of 40 mm and dipped in liquid nitrogen for 5 min to become solidified and then subjected to vacuum assisted freeze drying for a longer period.

To fabricate the required hybrid, the solution of mixed ions was stirred in the suspension of V_2C-MX sheets. The added Ni^{+2}, Fe^{+3}, Cr^{+3} ions could easily be anchored on the negatively charged MX surfaces via electrostatic interaction in DI-H_2O/ethylene glycol solution. Then, the NiFeCr were in situ grown on MXene sheets (NV-$_y$MX) under alkaline environment and heat flux. The etchant media in MX synthesis induced various anion functional groups such as OH^-, Cl^-, and F^- onto the surface of MX flakes and the as-prepared MXene possessed defects due to selective etching of the Al layers in a mixed HF:HCl solution. Thus, the as prepared MX attained tremendous surface energy and ideal surface sites for the adsorption of metal cations through electrostatic interaction in MXene/metal salts solution. Through the hydrolysis, NiFeCr nanosheets were nucleated and grew all over the surface of the V_2C MX substrate [35]. Thus, the addition of 3D crumpled MX regulated the growth and inhibited the undesired agglomeration of NiFeCr nanoflake forming an open structure of the hybrid with more accessible channels that are embellished with active sites for maximum adsorption of electrolytic ions as shown in Scheme 1 [36]. Clearly, this hybrid structure is more favorable for electrocatalytic reactions that could largely shorten mass diffusion and accelerate charge transfer process [37,38].

3.1. Structural analysis

X-ray diffraction (XRD) is conducted to probe the crystallographic features of synthesized materials. All the peaks of MAX V_2AlC phase have been indexed in Fig. 1A according to the (ICDD# 04-005-5222) with hexagonal p63/mmc unit cell structure. The XRD reflections of V_2CTx are quite different from those of V_2AlC precursor. A new diffraction peak at 7.8° appears, corresponding to the (002) planes of V_2CTx, while the characteristic reflections of V_2AlC at 13.6° (002) and 41.3° (103) are considerably weakened, indicating the effective etching of Al. Interestingly, such double reflection of (002) plane is the representative of two different interlayer spacings of the etched V_2C MX and the precursor. This reflection splitting is in good agreement with other experimental results [39–42]. The peak shifting to a lower angle supports an increased interlayer spacing (Supplementary Fig. S2A) with expanded c-lattice parameter confirming the successful formation of V–C–V two-dimensional 2D expanded conductive structure [43–45]. The c-lattice parameter of the hexagonal lattice structure obtained from the (002) plane has been increased by 13.1 Å for V_2AlC MAX phase to 22.4 Å V_2CTx MXene phase (Fig. S2B). Moreover, the highly reduced intensity of V_2AlC XRD peaks at 13.6° and 41.3° resembles small portion of partially etched V_2AlC [41,46,47]. Along with these, the occurrence of tiny reflections for Orthorhombic V_2O_5 (200) and (201) planes at $2\theta = 15.8°$ and 23.9° respectively in accordance with (ICDD# 04-015-2250), also contribute in enhancing the interlaminar spacing of MX [48]. The expanded lamelliform structure is due to successive etching of Al and intercalation of Et_3N spacer molecules during exfoliation of etched MX sheets, greatly advantageous for the diffusion of electrolyte ions. The distensible

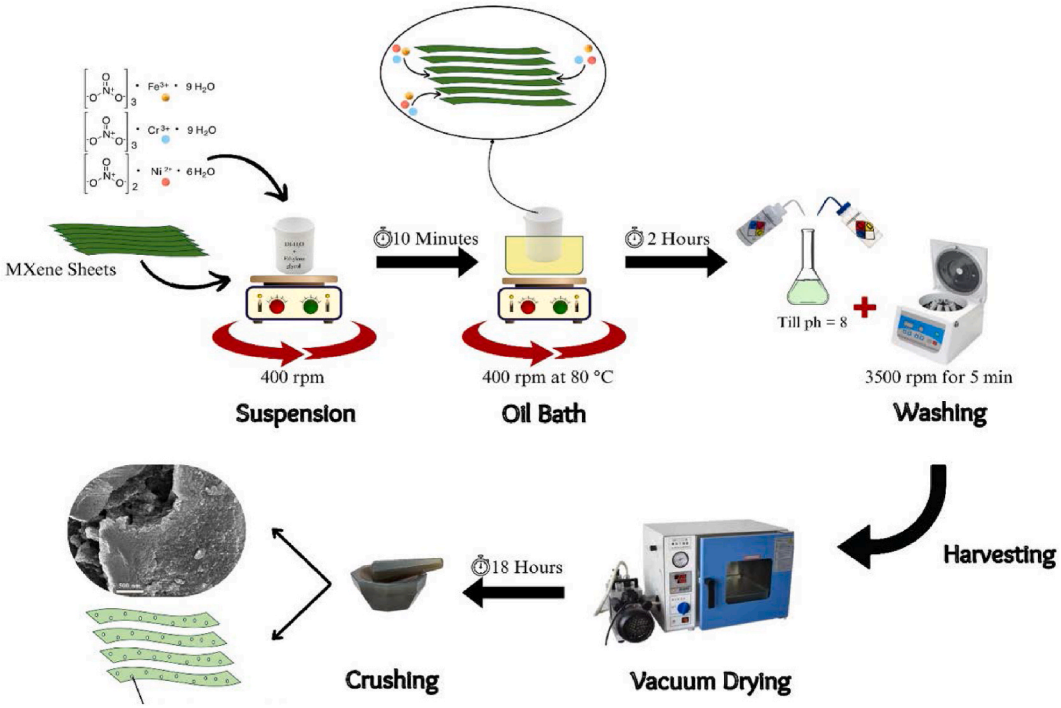

Schematics 1. Synthetic scheme for in-situ grown NiFeCr hydroxides on 3D crumpled MX substrate.

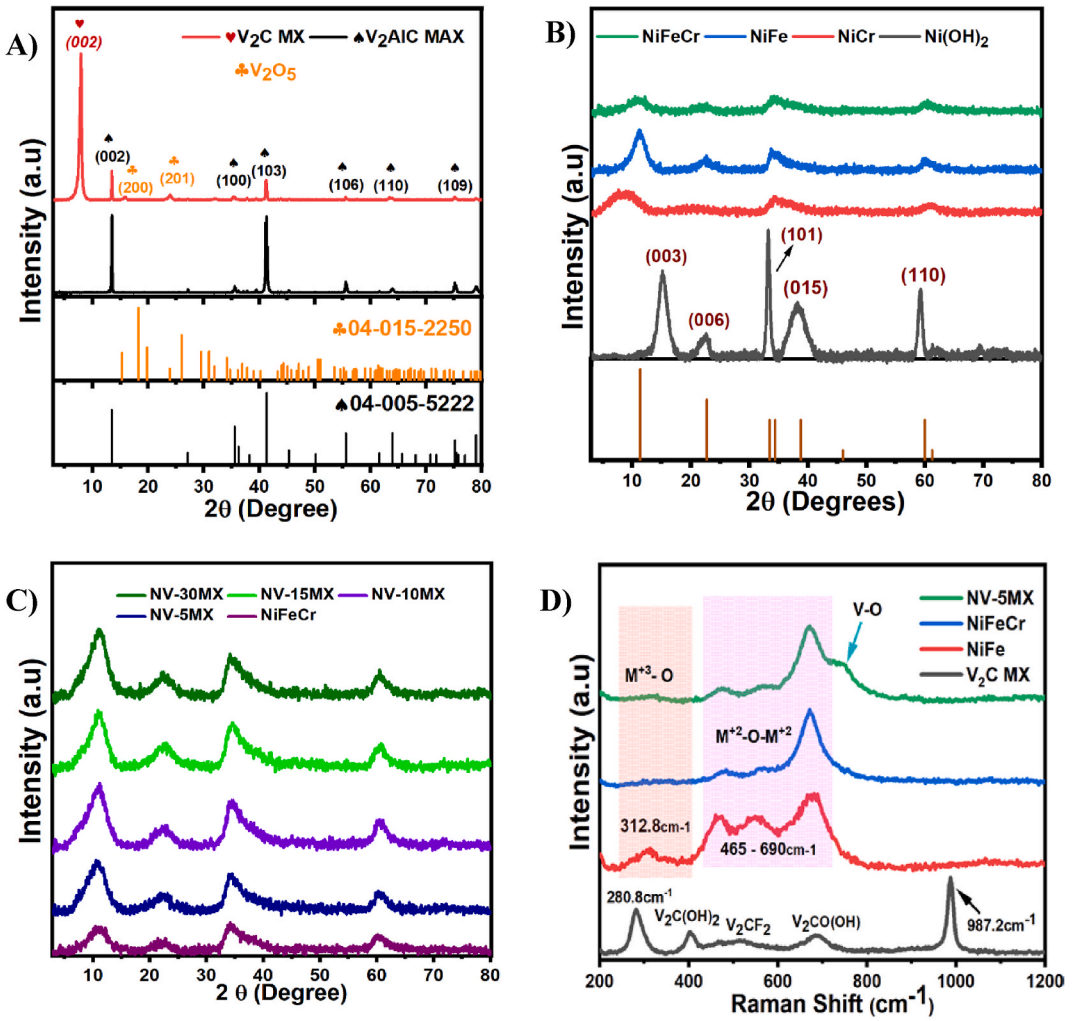

Fig. 1. XRD spectra of V_2AlC and V_2C MX spectra (A); XRD Spectra of $Ni(OH)_2$, NiFe, NiCr, and NiFeCr (B); XRD spectra of NV-*x*MX composites with different wt. percentages of MX (C), and Raman spectrum of V_2C MX, NiFe LDH, and NiFeCr (D).

interlaminar spacing of the MXene provide interlayer channels for maximum accessibility and rapid diffusion of electrolyte ions thus enhancing the electrochemical performance [45,49].

Powder X-ray diffraction (PXRD) patterns are used to confirm the structure and the phase purity of the synthesized metal hydroxides. The XRD pattern of synthesized $Ni(OH)_2$ (Fig. 1B) are well-matched with the α phase of $Ni(OH)_2$ (ICDD# 38–0715). The shift in peak position oriented at $2\theta = 15.0^\circ$ in comparison of the provided XRD pattern as a reference, can be attributed to the perturbed lattice dimensions due to intercalated water molecules and anions in the interlayer spacing of synthesized samples [50–52]. However, the considerable shift in peak positions have been observed for both NiCr and NiFe as compared to the peak positions for pristine Ni $(OH)_2$. Moreover, these peaks are weakened and broadened, indicating the low crystallinity of NiCr and NiFe LDH (Fig. 1B) [53]. The calculated crystallite sizes from the reflections (003), (006), (101), (015), and (110) are found as 6.79, 2.09 and 3.09 nm for α -Ni $(OH)_2$, NiCr and NiFe LDHs respectively. Moreover, the increased crystallite size of NiFe LDH is supported by the greater intensity of diffractions peaks as compared to NiCr which might be due to different ionic radius of cations such as 69 p.m., 62pm, and 55 p.m. for Ni^{+2}, Cr^{+3}, and Fe^{+3} [54]. For NiFeCr catalyst, the same diffraction peaks are greatly suppressed and broadened as compared to NiFe (Fig. 1B), which indicates the reduced particle size and the formation of homogeneous amorphous structure. Therefore, the substitution of more types of metal elements causes lattice perturbation that leads to an amorphous structure with fluctuated internal ionic field energy, strain effect and enriched defects to enhance the electrocatalytic OER performance [55,56]. The X-Ray diffraction pattern of NiFeCr grown on MX sheets (Fig. 1C) indicate that the characteristic peaks of NiFeCr do not significantly shift with respect to the different contents of V_2C MXene sheets in NV-*y*MX composites. Furthermore, there is no individual MXene reflections in the whole XRD patterns of NV-*y*MX composites even upon increased dosage of V_2C Mxene sheets. This supports the effective homogenous intergrowth of NiFeCr in-between the interlayer channels of MXene sheets. However, the XRD peaks of NiFeCr in NV-*y*MX hybrid are greatly prominent than in the pure NiFeCr that indicates the increased crystalline size of hybrid within the range of 2.84 nm–2.95 nm as

compared to 2.36 nm crystallite size of pure NiFeCr as shown in (Fig. S2C). This could be attributed to the terminal functional groups (–F, –OH, -Cl, and –O) of MX, which triggered the adsorption of metal cations and hence supported the orientated growth of NiFeCr [57,58]. Fig. 1D shows the Raman spectra of synthesized V_2C MX, NiFe LDH, and NV-5MX electrocatalysts within the range of 200–1200 cm^{-1}. In the Raman spectrum of V_2C MX, the peak occurring at 280.8 cm^{-1} and 987.2 cm^{-1} correspond to vibrations of V–C [59] whereas the peak at 401.1 cm^{-1} is originated from $V_2C(OH)_2$. Similarly the bands at ~518.4 cm^{-1} and ~687.9 cm^{-1} are referred to out-of-plane vibration of V atoms in V_2CF_2 and $V_2CO(OH)$ chemical species, respectively [45,59]. Such vibrational signals assure the successful etching of MAX phase into MX embellished with–OH, –O, and –F functional groups [60]. The Raman spectra of multi-metal hydroxides and NV-$_y$MX composites (Fig. 1D), exhibit the presence of all O-M-O bending modes that include $M^{III}/M^{II}–O–M^{II}$ and $M^{III}–O–M^{III}$ bonds within the range of 300 and 700 cm^{-1} [61,62]. In the case of NiFeCr hydroxides the shifting of some parental peaks of NiFe LDH toward lower wavenumbers with reduced intensity suggests the distortion in the crystal structure of NiFe LDH due to effective incorporation of Cr ions as evident in the findings of X-Ray Diffraction [63]. In addition to $Ni^{+2}/Fe^{+3/}Cr^{+3}$-O bonds, there is an extra shoulder peak centred around 750 cm^{-1} in NV-5MX corresponds to the stretching modes of V–O bonds in oxy-vanadate species such as V_3O and $(V_2O_2)_n$ [64,65]. Interestingly, in accordance with the reported literature, there is no evidence of V–C bond vibrations in NV-5MX due to the low percentage of V_2C MX sheets [66]. These obtained structural features via XRD and Raman guarantee the effective combination of trimetallic hydroxides and V_2C MX, which considerably regulate the growth of trimetallic hydroxides at conductive MX substrates with suppressed agglomeration for increased charge transfer process during OER [30].

3.2. Morphological analysis

Field emission scanning electron microscopy (FESEM) is applied to analyze the morphological features of the synthesized materials (Fig. 2A–D). The FESEM of the MAX V_2AlC powder shows the morphology of typical close-packed laminated bulk particles (Fig. 2A), while Fig. 2B shows the FESEM image of V_2C MX, illustrating a highly crumpled microporous scaffold. The crinkly sheets with bent and curved edges are randomly oriented into a three-dimensional (3D) framework. The interconnected walls of multilayers formulate the porous structure as presented in the Supplementary Fig. 3SA. The well-retained 3D structure of self-oriented V_2C MX is attributed to the slow sublimation of ice during the freeze-drying process [67]. This is inherently different from the commonly observed parallel-stacked MX sheets obtained through vacuum-filtration [15,68]. The large agglomerates with plate like morphology of NiFeCr

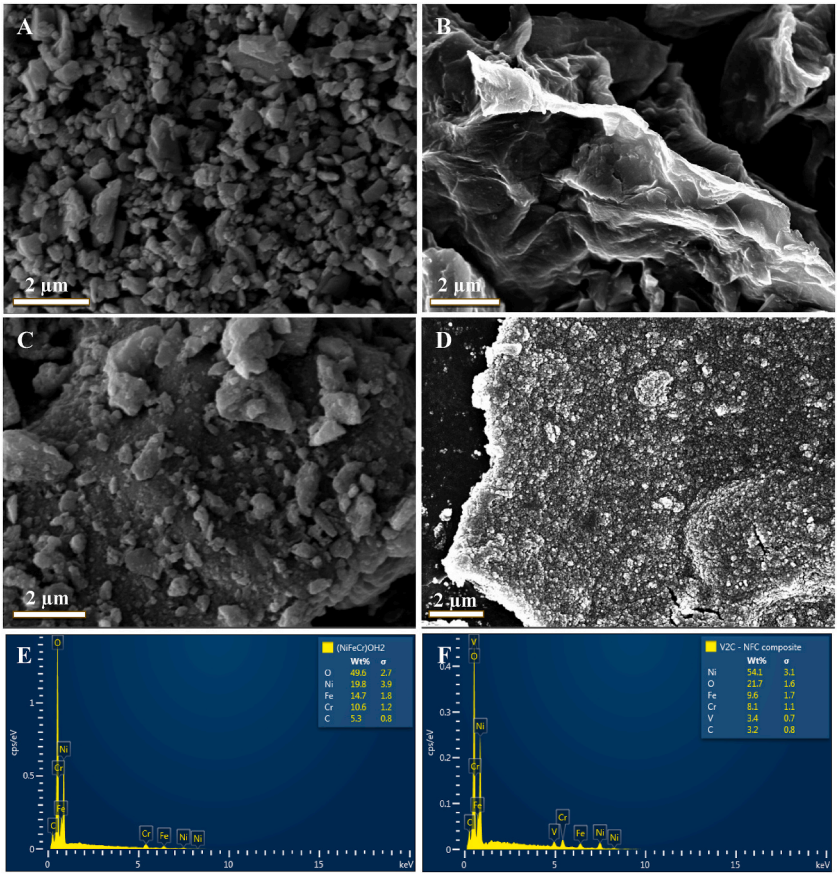

Fig. 2. The FESEM images of V_2AlC (A), V_2C MX (B), NiFeCr (C), and NV-5MX (D); The EDX spectra of NiFeCr (E), and NV-5MX (F).

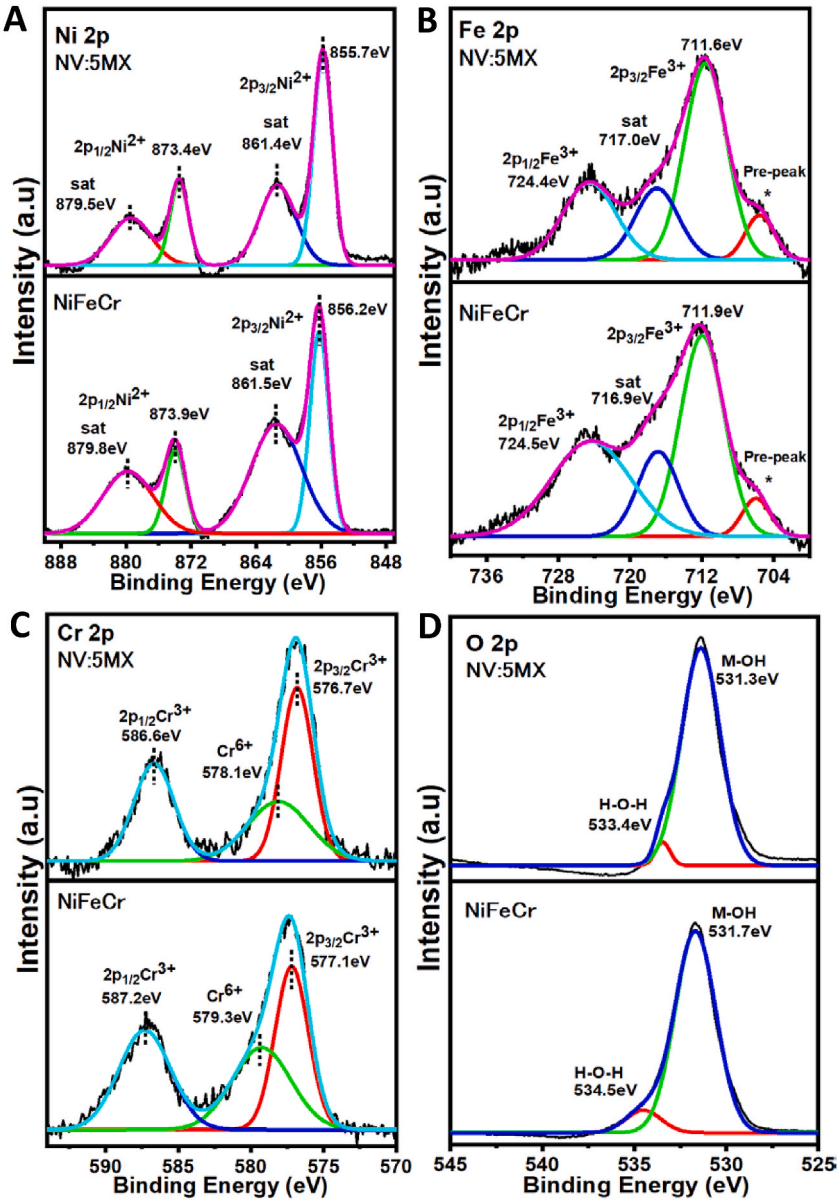

Fig. 3. XPS Spectra of Ni 2p (A), Fe 2p (B), Cr 2p (C), and O 2p (D) electrons in NiFeCr and NV:5MX.

are observed in the absence of V_2C MX (Fig. 2C). In contrast, when NiFeCr are in-situ grown on V_2C MX sheets to form NV-5MX hybrid, the morphology of NiFeCr has been changed into near-spherical shaped and are much smaller and uniformly dispersed over V_2C MX sheets, indicating the controlled growth of NiFeCr particles during the in-situ synthesis of NiFeCr over 3D crumpled V_2C MX sheets. The role of MXene substrate in the formation of small size and well dispersed metal hydroxides is also evident in the related literatures [30, 69]. Moreover, the unique 3D morphological features of V_2C MX offer significantly enhanced surface sites for the growth of NiFeCr particles. Consequently, the NV-5MX hybrid illustrates the embellishment of NiFeCr on all sides of the crumpled walls as marked in Supplementary Fig. 3SB, demonstrating an opened structure for the maximum adsorption of electrolytic ions [27]. Elemental composition of all synthesized materials has been determined through EDX spectra. The prominent reduction of Al percentage in EDX spectra of V_2C MX (Supplementary Fig. 4Sa) has been observed as compared to the percentage of Al in EDX spectra of MAX phase (Fig. 4Sb) as evident in the aforementioned XRD results. The EDX spectra (Fig. 4Sa) assures the presence of terminal functionalities with F and Cl in V_2C MX after etching of V_2AlC MAX phase. It must be kept into consideration that O and/or OH terminal groups are also present in V_2C MX scaffold, but the observance of O content was not possible which might be due to overlapped peaks of O and V [70]. Fig. 2e confirms the presence of desired elements Ni, Fe, Cr, and O in trimetallic NiFeCr hydroxide; similarly, V can be prominently observed in EDX spectra of NV-5MX (Fig. 2f). However, there is no evident peak of Al, F, and Cl in the EDX spectrum of NV-5MX which might be due to high coverage of NiFeCr metallic centers over relatively low amount of V_2C MX sheets as found in agreement

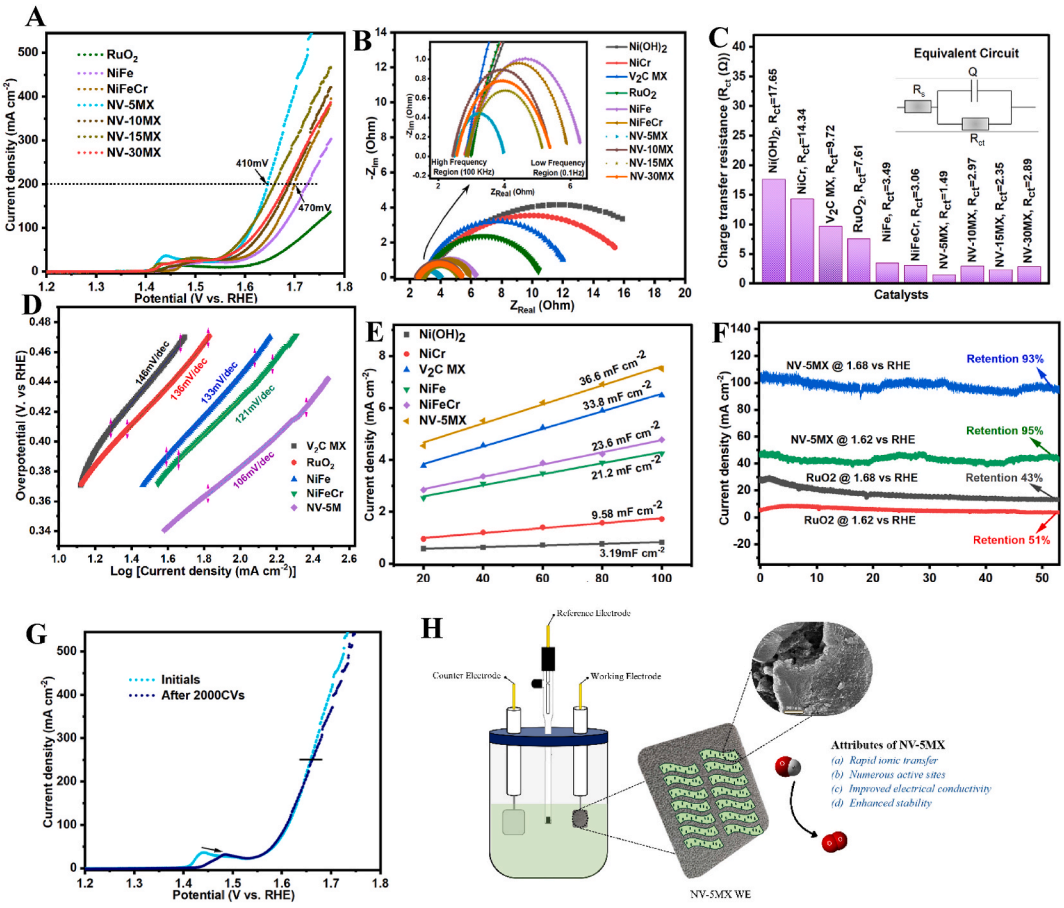

Fig. 4. Electrochemical Oxygen evolving performance of NV-yMX hybrids, The LSV curves of the prepared catalysts (A), EIS spectra of all synthesized catalysts from high frequency range to low frequency range (B), An overview of charge transfer resistance values obtained through Randles circuit (C), TAFEL slopes showing the kinetics of pristine V_2C MX, RuO_2, NiFe, NiFeCr, and NV-5MX composite (D), C_{dl} plots (E), Long-term stability evaluation at different OER active voltages (F), and Post LSV curve of NV-5M after 2000CV cycles (G), (H) Schematic representation of 3D electrode setup used for investigating the OER electrochemical kinetics at NV-MX based electrode.

with the literature [30,66,69,71].

3.3. Chemical analysis

XPS is a surface chemical analysis technique commonly used to evaluate the electronic structure of the synthesized materials. The high-resolution Ni 2p XPS spectrum of NiFeCr (Fig. 3A), confirms the presence of bivalent Ni^{+2} with the characteristic peaks at binding energies of 856.2eV and 873.9eV correspond to the $Ni2p_{3/2}$ and Ni $2p_{1/2}$ respectively along with their satellite peaks at 861.5eV and 879.8eV [72,73]. The negative shifts in the characteristic Ni2p peaks have been observed for NV:5MX (Fig. 3A) [27,74]. In Fe 2p spectra of NiFeCr (Fig. 3B) other than the satellite peaks at 716.9 eV and pre-peak at low energy due to defects, the characteristic peaks at 711.9eV, and 724.5eV due to $2p_{3/2}Fe^{+3}$, and $2p_{1/2}Fe^{+3}$ respectively, are also prominent [24,52,75,76]. Similar, negative shifts have been observed in these characteristic peaks for $2p_{3/2}Fe^{+3}$, and $2p_{1/2}Fe^{+3}$ in NV:5MX (Fig. 3B) [24,77]. In Fig. 3C, the Cr 2p spectrum in NiFeCr manifests three characterisation peaks Cr^{+3} $2p_{3/2}$ (577.1eV), Cr^{+3} $2p_{1/2}$ (587.2 eV), and Cr^{6+} (579.3 eV) indicating the mixed valence states of Cr^{+3} and Cr^{+6} in the catalyst [78]. In comparison of NiFeCr, the Cr 2p peaks of NV:5MX are shifted to lower energy values (Fig. 3C) ensuring the strong electronic interaction between transition metal hydroxides and MX sheets [7]. The negative shift in the binding energies of active metal ions demonstartes the charge compensation between metal cations due to electronegativity (EN) difference. The denoted electrons from Vanadium ions to the surrounding Ni, Fe, and Cr ions resulted into electron-rich metallic centers. Such electron-rich structure with reduced binding energy of active metal cations in NV:5MX supports the improved OER activity affecting the de-protonation step in the OER by strengthening the binding affinity between the adsorbates and the active sites [79–81]. Specifically, the O1s spectra (Fig. 3D) of NiFeCr illustrates two peaks at 531.7eV, and 534.5eV corresponding to M − OH bond and chemisorbed H_2O on the catalyst surface [78], while the negative shifts in the binding energy of M − OH bond has been appeared for NV:5MX leading the enhancement of active sites at the phase interface [82]. The XPS spectrum of V 2p (Fig. 5S) exhibits characteristic peak of V–C at 513.5eV, V^{+4} $2p_{3/2}$ at 516.6eV, and V^{+4} $2p_{1/2}$ at 524.0eV in as-synthesized V_2C Mxene [72,73,83] whereas in

NV:5MX, V^{+4} $2p_{3/2}$ and V^{+4} $2p_{1/2}$ peaks (Fig. 5S) have been shifted to higher energies reflecting the reconstructed electron density in the vicinity of trimetallic hydroxides ensuring strong chemical interaction between trimetallic hydroxides and inserted V_2C MX sheets [73,84].

3.3.1. Electrochemical Oxygen evolution Assessment

Based on the physiochemical properties, the OER performance of all synthesized electrocatalysts have been compared with the commercially purchased RuO_2, in terms of overpotential at higher current density, charge transfer resistance, electrochemical surface area, and Tafel slopes. Fig. 4A displays the linear sweep voltammetry (LSV) polarization curves of NiFeCr/MXene (NV-$_y$MX) hybrids with different wt.% of MX contents, NiFe, NiFeCr, and RuO_2. From the LSV curves the deduced overpotential of NV-5MX is 410 mV, which is smaller than NV-15MX (430 mV), NV-30MX (440 mV), NV-10MX (450 mV), NiFeCr-LDHs (470 mV), and NiFe-LDHs (500 mV) respectively, at a current density of 200 mA cm^{-2}. All the NV-MX catalysts show better OER activity than pristine NiFeCr-LDHs electrode. As plotted in Supplementary Fig. 6S, the Ni foam substrate exhibits very least OER current density, whereas OER activities of binary metal hydroxides NiCr and NiFe have been improved at higher voltages as compared to pristine unarymetal hydroxide $Ni(OH)_2$. The NiFe-LDHs showed significantly reduced OER over potential (400 mV) in comparison to RuO_2 (450 mV) and V_2C-MX (470 mV) at current densities of 50 mA cm^{-2}. Furthermore, electrochemical impedance spectroscopy (EIS) is performed to investigate the charge transfer kinetics of all the synthesized electrocatalysts. At set overpotential of 500 mV, semicircles are obtained in the Nyquist plots Fig. 4B of all synthesized electrocatalysts, describing the electron-conduction impedance. In electrochemical impedance spectroscopy, the narrower diameter of the semicircle reflects the faster charge transfer kinetics [85,86]. The prominently low semicircle diameter of NV-5MX as compared to all synthesized materials, indicates considerably suppressed charge-transfer resistance (R_{ct}) and favorable electrokinetics. The R_{ct} value of NV-5MX (1.49Ω) compared with those of $Ni(OH)_2$ LDH ($R_{ct} = 17.65Ω$), NiCr-LDHs ($R_{ct} = 14.34Ω$), V_2C MX ($R_{ct} = 9.72Ω$), RuO_2 (7.61Ω), NiFe-LDHs ($R_{ct} = 3.49Ω$), NiFeCr-LDHs ($R_{ct} = 3.06Ω$), NV-15MX ($R_{ct} = 2.35Ω$), NV-30MX ($R_{ct} = 2.89Ω$), and NV-10MX ($R_{ct} = 2.97Ω$) shown in Fig. 4C, is in accordance with the sequence of their OER performances. The kinetics of the electrocatalyst reactions are extracted from the LSV polarization curves using Tafel plots. NV-5MX shows a low value of Tafel slope of (106 mV dec^{-1}) in comparison of V_2C (146 mV dec^{-1}), RuO_2 (136 mV dec^{-1}), NiFe (133 mV dec^{-1}), and NiFeCr (121 mV dec^{-1}) (Fig. 4D), suggesting the improved reaction kinetics of OER process [74]. The electrochemical surface area (ECSA) presented in Supplementary Figs. 7S(a–f) of synthesized materials are utilized to provide the intrinsic catalytic features by evaluating the electrochemical double-layer capacitance (C_{dl}) through a cyclic voltammetry (CV) method. As found in Fig. 4E, the NV-5MX presents the highest C_{dl} value (36.6 mF cm^{-2}) than V_2C MX (33.8 mF cm^{-2}), NiFeCr (23.6 mF cm^{-2}), NiFe (21.2 mF cm^{-2}), NiCr (9.58 mF cm^{-2}), and $Ni(OH)_2$ (3.19 mF cm^{-2}). It should be pointed out that the V_2C MX shows the greater C_{dl} value than NiFeCr which might be due to the porous morphological features. Therefore, LSV curves of V_2C MX, NiFeCr, NV-5MX were normalized by the corresponding ECSA values (Supplementary Fig. 8S) in order to evaluate their intrinsic OER activities and found the same trend of OER activity [72,87]. Besides, the electrochemical durability of an electrocatalyst is also crucial. For this stability test, NV-5MX, and RuO_2 were subjected to chronoamperometric test (Fig. 4F) for more than 50 h at non-iR corrected 1.62V vs RHE and 1.68V vs RHE potentials respectively. Upon 53 h of long OER performance NV-5MX holds the 95 % current density whereas RuO_2 holds 51 % of initial current density at 1.62V. Similarly at higher overpotential values 1.68V, for higher current densities the NV-5MX still shows 93 % current retention, on the other hand, RuO_2 retains only 43 % of initial current density. Interestingly, NV-5MX possess the regenerative current behaviour during long period OER performance whereas RuO_2 presented a continuous decay in current density. Such regenerated activity during continuous OER operation signifies that the active sites in NV-5MX have greater possibilities to interact with the electrolyte solution, thus causing the faster ionic OH transportation and strengthening the electrode reaction during the OER process. Despite the massive release of O_2 at electrode surface, the interaction between active metallic centers and the MXene support prevent detachment or agglomeration of active centers that improves the effect of MXene matrix for fast and stable electron transfer channels during the long-term OER electrocatalytic process [88–91]. Moreover, the current density of NV-5MX electrode nearly remains the same and shows a negligible decay at higher over potential region (Fig. 4g) after 2000 repeated CV cycles within the OER active region, however there is a positive drift of 40 mV in the Ni redox peak. Such peak shift in more anodic region can be associated with the in-situ formed oxidative passive layer at NV-5MX catalyst surface during continuous OER. Fundamentally, the in-situ formed passive layer modifies the surface charge density of the electrode and governs the adsorption kinetics of the electrolytic ions thus affecting the peak shape and position [92].

The improved order of OER electrocatalytic activity of the electrocatalysts ($Ni(OH)_2$ < NiCr < V_2C MX < RuO_2<NiFe < NiFeCr < NV-10MX < NV-30MX < NV-15MX < NV-5MX) can be ascribed to the synergistic electronic interaction among 3D crumpled V_2C-MX framework and hetero-nuclei metallic ions. The highly conductive V_2C-MX nanosheets can considerably suppress the charge transfer resistance in a hybrid electrocatalyst to yield a greater number of triple-phase boundaries for accelerated OER kinetics. The highly dispersed NiFeCr are immobilized on open pores of V_2C-MX exposing massive metal atoms at inner/outer surface sites and edge positions thus provides sufficiently accessible active sites for improved electrocatalytic performance. Moreover the impede agglomeration of active sites and enhanced redox activity of mixed metal cation centers ensure the outstanding stability of synthesized catalyst [93]. Finally, the synergistic chemical interaction of active metallic centers with 3D crumpled MX scaffold induces dominant electron transfer between NiFeCr and V_2C-MX nanosheets that could greatly improve the intrinsic catalytic properties of the hybrid. Fig. 4H provides the schematic representation of activity and stability of NV-MX electrodes in alkaline media.

4. Conclusion

In summary, we report a facile synthetic protocol based on in-situ ammonia assisted liquid-phase coprecipitation of NiFCr on 3D

crumpled MX sheets in an open oil bath for NV-*y*MX electrocatalysts with different loadings of V_2C MX sheets. Owing to a coupled effect of the conductive V_2C-MX and OER-active NiFeCr, the NV-MX hybrid showed an eximious electrocatalytic activity with an overpotential of 410 mV at a current density of 200 mA cm^{-2} and Tafel slope of 100 mV dec in 1MKOH indicating a considerably improved performance in comparison of pure NiFeCr, and RuO_2. Meanwhile, NV-MX hybrid demonstrated adequate stability during 53h of continuous OER process. A variety of characterization techniques such as XPS, RAMAN, XRD, and FESEM are employed to unveil the influencing factors for an improved OER electrochemical activity of NV-MX hybrid that can be listed as follows: the 3D crumpled framework of V_2C MX sheets provides an open pore like structure for nucleation of electrochemically OER active NiFeCr at inner/outer surface sites and around edges of the sheets. The NV-$_y$MX hybrid endows suitable crystallinity for effective charge transfer process at triple-phase boundaries. Besides, the synergy of well-dispersed dense coverage of hetero-metallic nuclei within the 3D network of crumpled V_2C-MX sheets effectively lowers the overpotential and induces appreciable stability of composite at higher current densities. This work provides significant insights into designing advanced MXene architectures as a catalyst support to anchor hetero-nuclei metallic ions for improved OER kinetics.

Data availability statement

Data associated with this study has not been deposited into a publicly available repository. Data will be made available upon request.

CRediT authorship contribution statement

Anum Iqbal: Writing – review & editing, Writing – original draft, Visualization, Validation, Software, Methodology, Investigation, Formal analysis, Data curation, Conceptualization. **Hamzeh Sabouni:** Writing – review & editing, Visualization, Validation, Software, Formal analysis, Data curation. **Nasser M. Hamdan:** Writing – review & editing, Validation, Supervision, Resources, Project administration, Funding acquisition, Conceptualization.

Declaration of competing interest

The authors declare that they have no known competing financial interests or personal relationships that could have appeared to influence the work reported in this paper.

Acknowledgment

This work was funded by the American University of Sharjah with grants: FRG22-C-S67 and FRG23-C-S65. The work in this paper was also supported, in part, by the Open Access Program from the American University of Sharjah. The authors are thankful to the Centre for Advanced Material Research at the University of Sharjah. We also extend our gratitude to Dr. S.T. Senthilkumar at Centre for Advanced Material Research at the University of Sharjah for the useful discussions. This paper represents the opinions of the authors and does not mean to represent the position or opinions of the American University of Sharjah.

Appendix A. Supplementary data

Supplementary data to this article can be found online at https://doi.org/10.1016/j.heliyon.2024.e35643.

References

[1] J. Masa, C. Andronescu, W. Schuhmann, Electrocatalysis as the nexus for sustainable renewable energy: the gordian knot of activity, stability, and selectivity, Angew. Chem. Int. Ed. 59 (36) (2020) 15298–15312.
[2] A. Iqbal, O.M. El-Kadri, N.M. Hamdan, Insights into rechargeable Zn-air batteries for future advancements in energy storing technology, J. Energy Storage 62 (2023) 106926.
[3] Q. Liu, L. Wang, H. Fu, Research progress on the construction of synergistic electrocatalytic ORR/OER self-supporting cathodes for zinc–air batteries, J. Mater. Chem. A 11 (9) (2023) 4400–4427.
[4] M.-I. Jamesh, M. Harb, Tuning the electronic structure of the earth-abundant electrocatalysts for oxygen evolution reaction (OER) to achieve efficient alkaline water splitting–A review, J. Energy Chem. 56 (2021) 299–342.
[5] F. Song, et al., Transition metal oxides as electrocatalysts for the oxygen evolution reaction in alkaline solutions: an application-inspired renaissance, J. Am. Chem. Soc. 140 (25) (2018) 7748–7759.
[6] L. Zhou, et al., Host modification of layered double hydroxide electrocatalyst to boost the thermodynamic and kinetic activity of oxygen evolution reaction, Adv. Funct. Mater. 31 (15) (2021) 2009743.
[7] Y. Yang, et al., Highly active trimetallic NiFeCr layered double hydroxide electrocatalysts for oxygen evolution reaction, Adv. Energy Mater. 8 (15) (2018) 1703189.
[8] T.X. Nguyen, et al., High entropy promoted active site in layered double hydroxide for ultra-stable oxygen evolution reaction electrocatalyst, Chem. Eng. J. 466 (2023) 143352.
[9] P.F. Guo, et al., Heterostructural NiFeW disulfide and hydroxide dual-trimetallic core-shell nanosheets for synergistically effective water oxidation, Carbon Energy (2024) e532.
[10] K. Wan, et al., Sulfur-modified nickel selenide as an efficient electrocatalyst for the oxygen evolution reaction, J. Energy Chem. 62 (2021) 198–203.

[11] K. Wan, et al., Hierarchical porous Ni3S4 with enriched high-valence Ni sites as a robust electrocatalyst for efficient oxygen evolution reaction, Adv. Funct. Mater. 29 (18) (2019) 1900315.
[12] K. Wan, et al., Metal-organic framework-derived cation regulation of metal sulfides for enhanced oxygen evolution activity, Chin. J. Catal. 54 (2023) 290–297.
[13] J. Xu, et al., A strong coupled 2D metal-organic framework and ternary layered double hydroxide hierarchical nanocomposite as an excellent electrocatalyst for the oxygen evolution reaction, Electrochim. Acta 307 (2019) 275–284.
[14] I. Hussain, et al., MXene-based heterostructures: current trend and development in electrochemical energy storage devices, Prog. Energy Combust. Sci. 97 (2023) 101097.
[15] A. Iqbal, N.M. Hamdan, Investigation and optimization of mxene functionalized mesoporous Titania films as efficient photoelectrodes, Materials 14 (21) (2021) 6292.
[16] Y. Wang, et al., Challenges and opportunities in utilizing MXenes of carbides and nitrides as electrocatalysts, Adv. Energy Mater. 11 (3) (2021) 2002967.
[17] B.R. Anne, et al., A review on MXene as promising support materials for oxygen evolution reaction catalysts, Adv. Funct. Mater. 33 (51) (2023) 2306100.
[18] L. Hu, et al., Modulating interfacial electronic structure of CoNi LDH nanosheets with Ti3C2Tx MXene for enhancing water oxidation catalysis, Chem. Eng. J. 398 (2020) 125605.
[19] Z. Lv, et al., Induction of Co2P growth on a MXene (Ti3C2T x)-modified self-supporting electrode for efficient overall water splitting, J. Phys. Chem. Lett. 12 (20) (2021) 4841–4848.
[20] N. Li, et al., Synergistic phosphorized NiFeCo and MXene interaction inspired the formation of high-valence metal sites for efficient oxygen evolution, J. Mater. Sci. Technol. 106 (2022) 90–97.
[21] K.R.G. Lim, et al., Rational design of two-dimensional transition metal carbide/nitride (MXene) hybrids and nanocomposites for catalytic energy storage and conversion, ACS Nano 14 (9) (2020) 10834–10864.
[22] L. Trotochaud, et al., Nickel–iron oxyhydroxide oxygen-evolution electrocatalysts: the role of intentional and incidental iron incorporation, J. Am. Chem. Soc. 136 (18) (2014) 6744–6753.
[23] F. Dionigi, et al., In-situ structure and catalytic mechanism of NiFe and CoFe layered double hydroxides during oxygen evolution, Nat. Commun. 11 (1) (2020) 2522.
[24] M.H. Wang, et al., Operando high-valence Cr-modified NiFe hydroxides for water oxidation, Small 18 (19) (2022) 2200303.
[25] Y. Yang, et al., Enhancing water oxidation of Ru single atoms via oxygen-coordination bonding with NiFe layered double hydroxide, ACS Catal. 13 (4) (2023) 2771–2779.
[26] T. Zhang, et al., Boosting the oxygen evolution electrocatalysis of high-entropy hydroxides by high-valence nickel species regulation, Chem. Commun. 58 (55) (2022) 7682–7685.
[27] L. Yan, et al., Synergistically modulating the electronic structure of Cr-doped FeNi LDH nanoarrays by O-vacancy and coupling of MXene for enhanced oxygen evolution reaction, Int. J. Hydrogen Energy 48 (5) (2023) 1892–1903.
[28] X. Bo, et al., NiFeCr hydroxide holey nanosheet as advanced electrocatalyst for water oxidation, ACS Appl. Mater. Interfaces 9 (47) (2017) 41239–41245.
[29] K. Kawashima, et al., Accurate potentials of Hg/HgO electrodes: practical parameters for reporting alkaline water electrolysis overpotentials, ACS Catal. 13 (3) (2023) 1893–1898.
[30] X. Li, et al., Boosting oxygen evolution reaction by synergistically coupling amorphous high-entropy borate FeCoNiMnBOx with MXene, Appl. Surf. Sci. 645 (2024) 158838.
[31] A. Karmakar, S. Kundu, A concise perspective on the effect of interpreting the double layer capacitance data over the intrinsic evaluation parameters in oxygen evolution reaction, Mater. Today Energy 33 (2023) 101259.
[32] G. Li, et al., New insights into evaluating catalyst activity and stability for oxygen evolution reactions in alkaline media, Sustain. Energy Fuels 2 (1) (2018) 237–251.
[33] J. Orangi, et al., Conductive and highly compressible MXene aerogels with ordered microstructures as high-capacity electrodes for Li-ion capacitors, Materials Today Advances 9 (2021) 100135.
[34] Z. Chen, et al., Porous NiFe alloys synthesized via freeze casting as bifunctional electrocatalysts for oxygen and hydrogen evolution reaction, Int. J. Hydrogen Energy 46 (76) (2021) 37736–37745.
[35] S. Venkateshalu, et al., Synergistic MXene/LDH heterostructures with extensive interfacing as emerging energy conversion and storage materials, J. Mater. Chem. A 11 (27) (2023) 14469–14488.
[36] H. Hong, et al., Surface-functionalized three-dimensional MXene supports to boost the hydrogen evolution activity of Pt catalysts in alkaline media, J. Mater. Chem. A 11 (10) (2023) 5328–5336.
[37] A. Sikdar, et al., Hierarchically porous 3D freestanding holey-MXene framework via mild oxidation of self-assembled MXene hydrogel for ultrafast pseudocapacitive energy storage, ACS Nano 18 (4) (2024) 3707–3719.
[38] X. Zhang, et al., 3D crinkled MXene/TiO2 heterostructure with interfacial coupling for ultra-fast and reversible potassium storage, J. Mater. Chem. A 12 (13) (2024) 7598–7604.
[39] F.H.s. Fagerli, et al., Removing fluoride-terminations from multilayered V2C T x MXene by gas hydrolyzation, ACS Omega 7 (27) (2022) 23790–23799.
[40] X. Guo, et al., Constructing P-doped self-assembled V 2 C MXene/NiCo-layered double hydroxide hybrids toward advanced lithium storage, Materials Advances 4 (6) (2023) 1523–1533.
[41] R. Thakur, et al., Insights into the thermal and chemical stability of multilayered V 2 CT x MXene, Nanoscale 11 (22) (2019) 10716–10726.
[42] S. Fatima, et al., Synthesis and characterization of erbium decorated V2CTx for water splitting properties, Int. J. Hydrogen Energy 55 (2024) 110–117.
[43] H. Xu, et al., V2C MXene enriched with-O termination as high-efficiency electrocatalyst for lithium-oxygen battery, Appl. Mater. Today 27 (2022) 101464.
[44] M. Shekhirev, et al., Characterization of MXenes at every step, from their precursors to single flakes and assembled films, Prog. Mater. Sci. 120 (2021) 100757.
[45] M.S. Mohseni-Salehi, et al., Effect of temperature and atmosphere on V2AlC etching for V2CTx MXenes synthesis used as anode for Li-ion storage systems, J. Energy Storage 66 (2023) 107462.
[46] Q. Shan, et al., Two-dimensional vanadium carbide (V2C) MXene as electrode for supercapacitors with aqueous electrolytes, Electrochem. Commun. 96 (2018) 103–107.
[47] Y. Liu, et al., In-situ electrochemically activated surface vanadium valence in V2C MXene to achieve high capacity and superior rate performance for Zn-ion batteries, Adv. Funct. Mater. 31 (8) (2021) 2008033.
[48] Y. Zhou, et al., Novel strain engineering combined with a microscopic pore synergistic modulated strategy for designing lattice tensile-strained porous V2C-MXene for high-performance overall water splitting, ACS Appl. Mater. Interfaces 15 (12) (2023) 15797–15809.
[49] N. Mahar, A. Al-Ahmed, A.A. Al-Saadi, Synthesis of vanadium carbide MXene with improved inter-layer spacing for SERS-based quantification of anti-cancer drugs, Appl. Surf. Sci. 607 (2023) 155034.
[50] X. Bo, et al., Operando Raman spectroscopy reveals Cr-induced-phase reconstruction of NiFe and CoFe oxyhydroxides for enhanced electrocatalytic water oxidation, Chem. Mater. 32 (10) (2020) 4303–4311.
[51] M. Wilhelm, et al., Ni-Fe layered double hydroxides for oxygen evolution Reaction: impact of Ni/Fe ratio and crystallinity, Mater. Des. 212 (2021) 110188.
[52] J. Xie, et al., Partially amorphous nickel–iron layered double hydroxide nanosheet arrays for robust bifunctional electrocatalysis, J. Mater. Chem. A 6 (33) (2018) 16121–16129.
[53] A. Lobinsky, D. Dmitriev, V. Popkov, Novel route of NiCr-layered double hydroxide nanosheets synthesis on nickel foam as a bifunctional electrocatalyst for water splitting process, Int. J. Hydrogen Energy 48 (59) (2023) 22495–22501.
[54] S. Liu, et al., Heterostructure of NiFe@ NiCr-LDH for active and durable oxygen evolution reactions in alkaline media, Materials 16 (8) (2023) 2968.
[55] Y. Hu, et al., Single Ru atoms stabilized by hybrid amorphous/crystalline FeCoNi layered double hydroxide for ultraefficient oxygen evolution, Adv. Energy Mater. 11 (1) (2021) 2002816.

[56] H. Li, et al., Accelerated oxygen evolution kinetics on NiFeAl-layered double hydroxide electrocatalysts with defect sites prepared by electrodeposition, Int. J. Hydrogen Energy 44 (54) (2019) 28556–28565.
[57] M. Benchakar, et al., MXene supported cobalt layered double hydroxide nanocrystals: facile synthesis route for a synergistic oxygen evolution reaction electrocatalyst, Adv. Mater. Interfac. 6 (23) (2019) 1901328.
[58] C. Hao, et al., Interface-coupling of CoFe-LDH on MXene as high-performance oxygen evolution catalyst, Mater. Today Energy 12 (2019) 453–462.
[59] A. Yadav, et al., Structural engineering and carbon enrichment in V2CTx MXene: an approach for enhanced supercapacitive charge storage, J. Alloys Compd. 934 (2023) 167859.
[60] E. Ghasali, et al., Production of V2C MXene using a repetitive pattern of V2AlC MAX phase through microwave heating of Al-V2O5-C system, Appl. Surf. Sci. 542 (2021) 148538.
[61] B. Sriram, et al., Eutectic solvent-mediated synthesis of NiFe-LDH/sulfur-doped carbon nitride arrays: investigation of electrocatalytic activity for the dimetridazole sensor in human sustenance, ACS Sustain. Chem. Eng. 8 (48) (2020) 17772–17782.
[62] F. Tang, et al., Windowless thin layer electrochemical Raman spectroscopy of Ni-Fe oxide electrocatalysts during oxygen evolution reaction, J. Electroanal. Chem. 871 (2020) 114282.
[63] K. Bera, et al., Accelerating the electrocatalytic performance of NiFe–LDH via Sn doping toward the water oxidation reaction under alkaline condition, Inorg. Chem. 61 (42) (2022) 16895–16904.
[64] R.L. Frost, et al., A Raman spectroscopic study of the different vanadate groups in solid-state compounds—model case: mineral phases vésigniéite [BaCu3 (VO4) 2 (OH) 2] and volborthite [Cu3V2O7 (OH) 2· 2H2O], J. Raman Spectrosc. 42 (8) (2011) 1701–1710.
[65] R. Tang, et al., Exploring the coordination change of vanadium and structure transformation of metavanadate MgV2O6 under high pressure, Sci. Rep. 6 (1) (2016) 38566.
[66] D. Tyndall, et al., Understanding the effect of MXene in a TMO/MXene hybrid catalyst for the oxygen evolution reaction, npj 2D Materials and Applications 7 (1) (2023) 15.
[67] T. Yun, et al., Multidimensional Ti3C2T x MXene architectures via interfacial electrochemical self-assembly, ACS Nano 15 (6) (2021) 10058–10066.
[68] K. Matthews, et al., Guidelines for synthesis and processing of chemically stable two-dimensional V2CT x MXene, Chem. Mater. 34 (2) (2021) 499–509.
[69] Y. Liu, et al., MXene-supported NiMn-LDHs as efficient electrocatalysts towards enhanced oxygen evolution reactions, Materials Advances 3 (10) (2022) 4359–4368.
[70] K.L. Firestein, et al., Delaminated V2C MXene nanostructures prepared via LiF salt etching for electrochemical applications, ACS Appl. Nano Mater. 5 (9) (2022) 12117–12125.
[71] E. Mazhar, et al., Efficient hydrogen and oxygen evolution reactions by using the V2CT x@ Sm nanocomposite, Energy & Fuels 38 (11) (2024) 10087–10095.
[72] C.F. Du, et al., V4c3t x mxene: a promising active substrate for reactive surface modification and the enhanced electrocatalytic oxygen evolution activity, InfoMat 2 (5) (2020) 950–959.
[73] Y. Chen, et al., V2C MXene synergistically coupling FeNi LDH nanosheets for boosting oxygen evolution reaction, Appl. Catal. B Environ. 297 (2021) 120474.
[74] M. Yu, et al., Boosting electrocatalytic oxygen evolution by synergistically coupling layered double hydroxide with MXene, Nano Energy 44 (2018) 181–190.
[75] Q. Xiang, et al., Electrodeposition of Pt3Sn nano-alloy on NiFe-layered double hydroxide with “card-house” structure for enhancing the electrocatalytic oxidation performance of ethanol, ChemNanoMat 7 (3) (2021) 314–322.
[76] J. Wang, et al., Fe-doped Ni2P nanosheet array for high-efficiency electrochemical water oxidation, Inorganic chemistry 56 (3) (2017) 1041–1044.
[77] H. Zhu, et al., Ultrathin graphitic carbon nitride interface layer regulated nickel-iron oxyhydroxide stabilized on nickel foam for efficient oxygen evolution reaction, Colloids Surf. A Physicochem. Eng. Asp. (2024) 133614.
[78] A. Malek, Y. Xue, X. Lu, Dynamically restructuring NixCryO electrocatalyst for stable oxygen evolution reaction in real seawater, Angew. Chem. 135 (40) (2023) e202309854.
[79] D. Zhou, et al., NiCoFe-layered double hydroxides/N-doped graphene oxide array colloid composite as an efficient bifunctional catalyst for oxygen electrocatalytic reactions, Adv. Energy Mater. 8 (9) (2018) 1701905.
[80] D. Zhou, et al., Layered double hydroxide-based electrocatalysts for the oxygen evolution reaction: identification and tailoring of active sites, and superaerophobic nanoarray electrode assembly, Chem. Soc. Rev. 50 (15) (2021) 8790–8817.
[81] T. Huang, et al., High-performance oxygen evolution reaction via self-optimizing interface engineering with simultaneous activation of dual-sites of surface oxyhydroxides, Appl. Surf. Sci. 659 (2024) 159936.
[82] X. Wei, et al., Improved OER electrocatalytic performance of Co-MOF by forming heterojunction with lower-conductivityWO3 nanorods or Cr2O3 nanoparticles, Int. J. Hydrogen Energy 58 (2024) 1240–1248.
[83] P. Cai, et al., Electric-field harmony in V2C/V2O5 heterointerfaces toward high-performance aqueous Zn-ion batteries, Energy Storage Mater. (2023) 102835.
[84] P. Li, et al., Tuning electronic structure of NiFe layered double hydroxides with vanadium doping toward high efficient electrocatalytic water oxidation, Adv. Energy Mater. 8 (15) (2018) 1703341.
[85] S. Anantharaj, S. Noda, Appropriate use of electrochemical impedance spectroscopy in water splitting electrocatalysis, Chemelectrochem 7 (10) (2020) 2297–2308.
[86] A. Iqbal, et al., Characteristics of electrochemical energy storage materials in light of advanced characterization techniques, in: Encyclopedia of Smart Materials, Elsevier, 2021, pp. 15–25.
[87] S.I.P. Bakovic, et al., Electrochemically active surface area controls HER activity for FexNi100− x films in alkaline electrolyte, J. Catal. 394 (2021) 104–112.
[88] X. Wang, et al., A-site cation-ordering layered perovskite EuBa0. 5Sr0. 5Co2–x Fe x O5+ δ as highly active and durable electrocatalysts for oxygen evolution reaction, ACS Omega 5 (21) (2020) 12501–12515.
[89] Q. Xiang, et al., In situ vertical growth of Fe–Ni layered double-hydroxide arrays on Fe–Ni alloy foil: interfacial layer enhanced electrocatalyst with small overpotential for oxygen evolution reaction, ACS Energy Lett. 3 (10) (2018) 2357–2365.
[90] Y. Wen, et al., Synergistic cerium doping and MXene coupling in layered double hydroxides as efficient electrocatalysts for oxygen evolution, J. Energy Chem. 52 (2021) 412–420.
[91] D. Mladenović, et al., Tailoring metal-oxide-supported PtNi as bifunctional catalysts of superior activity and stability for unitised regenerative fuel cell applications, Electrochem. Commun. 124 (2021) 106963.
[92] A. Tahir, et al., Electronic and surface modifications of Ni–Co–Fe oxides: a catalyst with maximum exposure of Fe active sites for water electrolysis, ACS Applied Engineering Materials 1 (7) (2023) 1698–1710.
[93] H. Wu, et al., High-Entropy layered double hydroxides with highly adjustable components for enhancing electrocatalytic oxygen evolution, ACS Appl. Mater. Interfaces 15 (32) (2023) 38423–38432.